

# Effect of C–N Interaction on Hydrogen Embrittlement of 15Cr–15Mn–4Ni-Based Austenitic Stainless Steels



KYUNG-SHIK KIM, JEE-HYUN KANG, and SUNG-JOON KIM

Hydrogen diffusion and embrittlement in an austenitic steel with 0.2 wt pct carbon and 0.2 wt pct nitrogen were investigated. The simultaneous alloying of both carbon and nitrogen did not reduce hydrogen diffusivity more than single alloying of nitrogen due to the interaction between carbon and nitrogen. During tensile straining, a low density of cracks initiated at the grain boundaries at an early deformation stage. The cracks propagated either along the grain boundaries and twin boundaries, or the paths where  $\epsilon$  martensite was concentrated, which resulted in mixed intergranular and transgranular fracture modes. Still, the resistance to hydrogen embrittlement improved in comparison with the single alloying of either carbon or nitrogen due to enhanced austenite stability.

<https://doi.org/10.1007/s11661-021-06376-5>

© The Minerals, Metals & Materials Society and ASM International 2021

## I. INTRODUCTION

AUSTENITIC stainless steels are a promising material for hydrogen environmental use due to their high resistance to hydrogen embrittlement, which originates from the fcc structure.<sup>[1,2]</sup> However, these steels exhibit relatively low strength, and require expensive austenite stabilizers such as Ni to avoid strain-induced martensites which are vulnerable to hydrogen-induced cracking.<sup>[3,4]</sup> Carbon and nitrogen are often alloyed in the austenitic stainless steels to enhance strength and austenite stability as well as corrosion resistance.<sup>[5–8]</sup> However, alloying high content of nitrogen would induce a ductile-to-brittle transition<sup>[9]</sup> and an excessive concentration of carbon would actively form carbides at grain boundaries.<sup>[10]</sup> To overcome the detrimental effect of each element while maintaining the beneficial properties, high interstitial steels which contain both carbon and nitrogen were developed.<sup>[11]</sup> These steels provide an excellent combination of strength and ductility.<sup>[12,13]</sup> The enhanced ductility is claimed to originate from the concentration increase in free electrons due to the interaction of carbon and nitrogen which enhances the metallic character of the steels.<sup>[14]</sup>

The distribution of carbon and nitrogen atoms also changes by the C–N interaction. Fe–N and Fe–C alloys were reported to have an 180 deg configuration of nitrogen atoms and 90 deg configuration of carbon atoms with the solute atoms, respectively, but this disappeared in a Fe–C–N alloy.<sup>[15,16]</sup> It was proposed that such blocking the same interstitial atoms in the first two coordination spheres resulted in high thermodynamic stability in high interstitial steels.<sup>[16]</sup> Moreover, it is known that the short-range ordering in Fe–N alloys, and clustering in Fe–C alloys would induce planar slip during deformation.<sup>[17]</sup> It was also reported that the planar slip was more prominent in the austenitic steels with both C and N than in the steels with either C or N,<sup>[18]</sup> possibly due to the stronger short-range ordering in C + N steels.<sup>[16]</sup> Therefore, adding both C and N cannot be understood as a simple summation of the effects brought by alloying either C or N.

Hydrogen-induced degradation of tensile properties in austenitic stainless steels was found to be reduced by both carbon and nitrogen.<sup>[19,20]</sup> However, carbon and nitrogen exhibited both beneficial and detrimental effects. Carbon effectively delayed the crack initiation and propagation by strengthening the grain boundaries, but could not decrease the hydrogen diffusivity.<sup>[19]</sup> Nitrogen could decrease the hydrogen diffusivity but encouraged the crack initiation and propagation along grain boundaries.<sup>[20]</sup> Since the simultaneous alloying of carbon and nitrogen enhanced the properties of austenitic steels in comparison with the single alloying of C or N,<sup>[11–14]</sup> it may also effectively increase the resistance to hydrogen attack. Unfortunately, the effect of C–N interaction on hydrogen embrittlement has never been studied

KYUNG-SHIK KIM and SUNG-JOON KIM are with the Graduate Institute of Ferrous Technology, POSTECH, Pohang 37673, Republic of Korea. JEE-HYUN KANG is with the School of Materials Science and Engineering, Institute of Materials Technology, Yeungnam University, Gyeongsan 38541, Republic of Korea. Contact e-mail: jeekang@yu.ac.kr

Manuscript submitted March 4, 2021; accepted June 28, 2021.

Article published online July 15, 2021

This research aimed to investigate hydrogen diffusion behavior and consequent hydrogen embrittlement behavior in the steels with 0.2 wt pct of both carbon and nitrogen. For better understanding of the C–N interaction effect, previous results of the same base composition with single alloying were compared.<sup>[19,20]</sup> The results were used to propose a hydrogen embrittlement mechanism in terms of C–N interaction.

## II. MATERIALS AND METHODS

The austenite stainless steels for the study was based on 15Cr–15Mn–4Ni–0.3Si (wt pct) with 0.2 wt pct of both C and N was prepared (Table I). The alloys were produced through conventional induction melting, and homogenization was performed at 1200 °C for 2 hours. Then, the alloy was hot rolled to the thickness of 12 mm, machined, and solution treated at 1100 °C for 10 to 30 minutes. After the solution treatment, the microstructure was fully austenite, and the grain size was 50 to 60  $\mu\text{m}$ .

Sub-sized tensile specimens were machined in the rolling direction. The gauge dimension was  $6 \times 25 \times 1.5 \text{ mm}^3$ . The samples were polished mechanically with 2000 grit sand papers before the testing to eliminate the oxidation layers formed during the annealing process. Tensile behavior was measured by tensile testing (INSTRON 5982) under the constant crosshead speed ( $0.1 \text{ mm min}^{-1}$ ) which corresponded to the initial strain rate of  $6.67 \times 10^{-5} \text{ s}^{-1}$ .

Electro-chemical charging of hydrogen into the tensile specimens was performed in  $30 \text{ g L}^{-1} \text{ NaCl} + 3 \text{ g L}^{-1} \text{ NH}_4\text{SCN}$  aqueous solution with a Pt wire as a counter electrode. Constant current density ( $50 \text{ A m}^{-2}$ ) was applied for 48 hours at 90 °C. The solution was replaced after 24 hours. For thermal desorption analysis (TDA), Qmass (HTDS-003) was employed and only the gauge part of the hydrogen charged tensile specimens was used. The heating rate during TDA was  $100 \text{ }^\circ\text{C h}^{-1}$  and the temperature range was 25 to 800 °C. Hydrogen permeation testing was also conducted with a modified Devanathan–Stachurski permeation cell<sup>[21]</sup> to identify the effective diffusivity of hydrogen. The details of the test methods can be found in our previous reports.<sup>[19,20]</sup>

The microstructure deformation was observed with field-emission scanning electron microscope (FE-SEM, JSM-7100F), electron backscatter diffraction (EBSD) analysis, energy dispersive X-ray spectroscopy (XRD, D-8 Advance), and field-emission transmission electron microscope (FE-TEM, JEM-2100F). The specimens for

EBSD were prepared by mechanical polishing with colloidal silica, and those for XRD were prepared by electro-chemical polishing with 10 pct perchloric acid mixed with 90 pct acetic acid. For TEM, the deformed tensile specimens were mechanically ground to 100  $\mu\text{m}$  thickness, and were punched into 3 mm disks. Then they were jet-polished with the same electrolyte used for the XRD specimen preparation.

The atomic distribution of interstitial elements were observed with 3D atom probe (LA-WATAP). The specimens were prepared by a focused ion beam system (FIB/FIB-SEM, Helios, Hikari, UMS II). The bulk C2N2 specimen without deformation was electro-chemically etched with an aqueous solution of 10 pct oxalic acid before FIB to detect the location of grain boundaries.

## III. RESULTS

### A. Tensile Behavior

Introduction of both carbon and nitrogen enhanced the strength of the steels (Figure 1(a)). The yield strength (YS) and ultimate tensile strength (UTS) of C2N2 were 324 and 764 MPa, respectively. C2N2 with the highest content of interstitials, exhibited the highest YS owing to the strengthening effect of interstitials in solid solution. The UTS was also the highest in C2N2 in comparison with C2 and N2.

The tensile properties in C2N2 were degraded by hydrogen pre-charging. YS was not altered by hydrogen, but fracture elongation and UTS decreased. When the relative loss of elongation ( $\Delta A_{\text{rel}}$ ) was calculated as  $\Delta A_{\text{rel}} = (A_{\text{N}} - A_{\text{H}})/A_{\text{N}}$ , where  $A_{\text{N}}$  and  $A_{\text{H}}$  are the fracture elongations without and with hydrogen pre-charging, respectively,  $\Delta A_{\text{rel}}$  was 10.5 pct for C2N2, while it was 17.4 and 15.9 pct for C2 and N2, respectively. Moreover, the strain hardening rate (SHR) was smaller after hydrogen pre-charging than in non-charged samples (Figure 1(b)). The deviation of SHR between non-charged and pre-charged C2N2 started at an early stage of deformation as in the case of N2; however, it was not aggravated until the true strain  $\sim 0.2$ . With higher strain, the deviation grew wider as in C2 (Figures 1(c) and (d)). Furthermore, the overall deviation of SHR was smaller than in C2 and N2.

### B. Microstructure in Hydrogen-Affected Zone

The fracture surface showed that pre-charging of hydrogen caused brittleness at the sample edge (Figure 2). C2N2 went through ductile fracture without hydrogen (Figure 2(a)). Brittle fracture occurred near the surface where hydrogen was introduced, *i.e.*, hydrogen-affected zone. A mixture of intergranular and transgranular fracture was observed in the hydrogen-affected region (Figures 2(b) and (c)). The fracture mode did not depend on the depth. Also, the depth of this brittle fracture area varied from 40 to 70  $\mu\text{m}$ . In previous studies, N2 showed intergranular fracture, and C2 exhibited cleavage and quasi-cleavage fracture. Also,

**Table I. Chemical Composition (Wt Pct) of Austenitic Stainless Steels Used in This Study**

Alloy	Cr	Mn	Ni	Si	N	C
C2 <sup>[19]</sup>	14.9	15.0	4.0	0.29	0.004	0.21
N2 <sup>[20]</sup>	15.0	15.2	4.1	0.26	0.19	0.015
C2N2	15.1	15.3	4.0	0.33	0.21	0.20

Fe is balance.

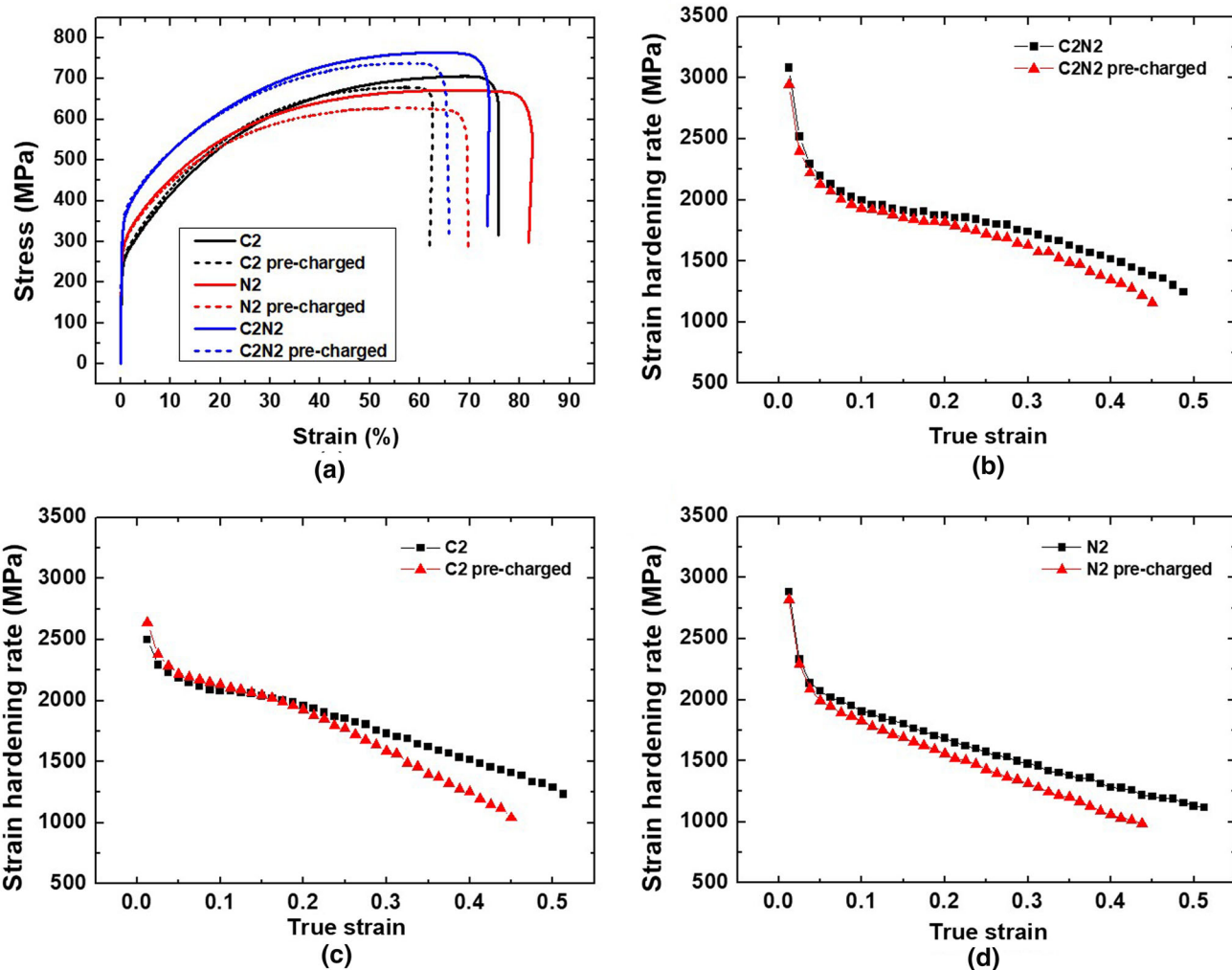


Fig. 1—(a) Tensile curves of C2N2, C2,<sup>[19]</sup> and N2<sup>[20]</sup> before and after hydrogen pre-charging, and strain hardening rate (SHR) curves with respect to true strain in (b) C2N2, (c) C2,<sup>[19]</sup> and (d) N2<sup>[20]</sup>

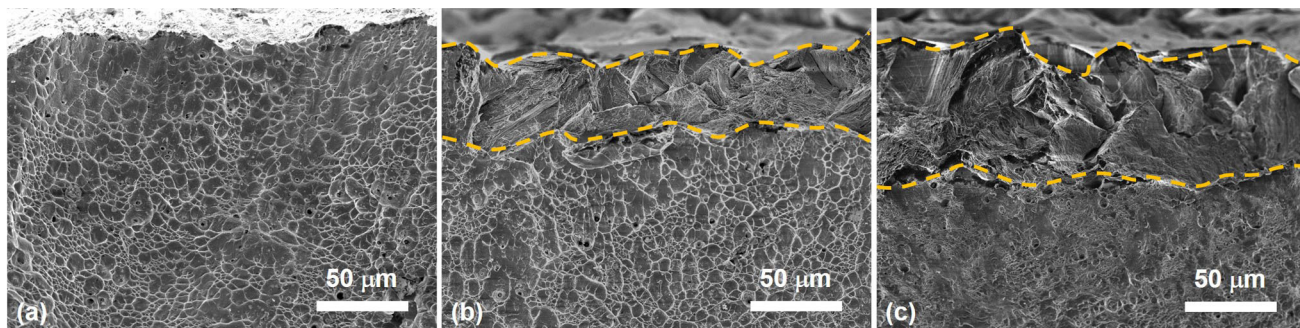


Fig. 2—The fractography of (a) non-charged C2N2 and hydrogen pre-charged C2N2 showing (b) minimum depth and (c) maximum depth of the hydrogen-affected region which was delineated by dotted lines. Note that the fractography was taken near the surface.

the depth varied for the brittle fracture in C2 but it did not in N2.<sup>[19,20]</sup>

The SHR deviation was the result of the surface cracking during deformation because the cracking would decrease the area that withstands the applied stress. When the surface of the pre-charged alloys were examined by interrupting the tensile straining (Figure 3),

few cracks were observed at the true strain of 0.1, which corresponded to the strain level where a small deviation in SHR arose (Figure 1(b)).

Both size and density of the cracks increased at the true strain of 0.2 (Figures 3(b) and (c)). Most of the crack initiation occurred at the grain boundaries, and seemed irrelevant to  $\epsilon$  martensite or the twin boundaries

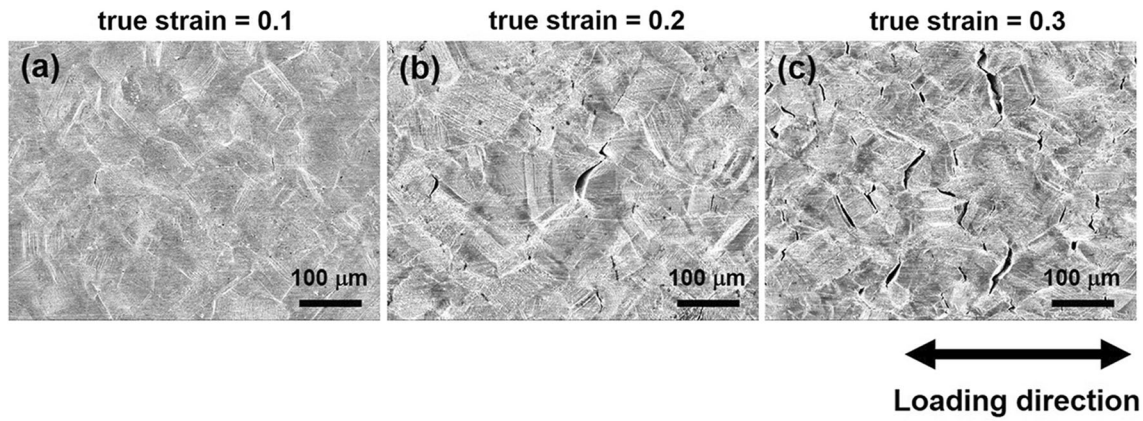


Fig. 3—Crack morphology at the side surfaces of pre-charged C2N2 samples at the true strain of (a) 0.1, (b) 0.2, and (c) 0.3.

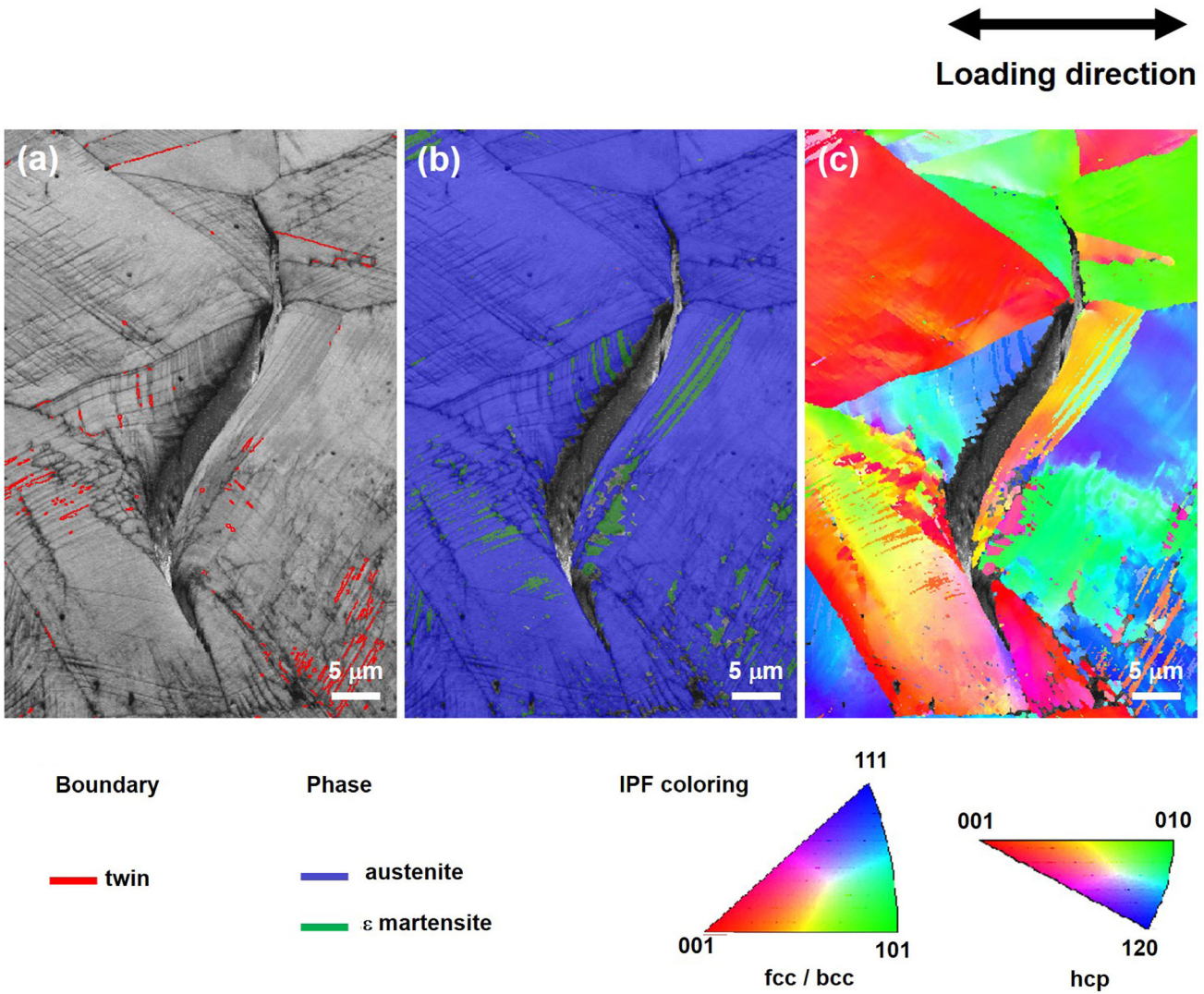


Fig. 4—Crack which appeared on the surface in pre-charged C2N2 at true strain = 0.2. (a) EBSD band contrast map showing twin boundaries, (b) phase map, and (c) IPF map.

(Figure 4). The cracks initiated at the surface propagated toward the center in two ways. In some cases, crack propagated along the grain boundaries without

adjacent  $\epsilon$  martensite (Figures 5(a) through (c)). This would result in intergranular fracture (Figures 2(b) and (c)). In other cases, cracks grew along the twin

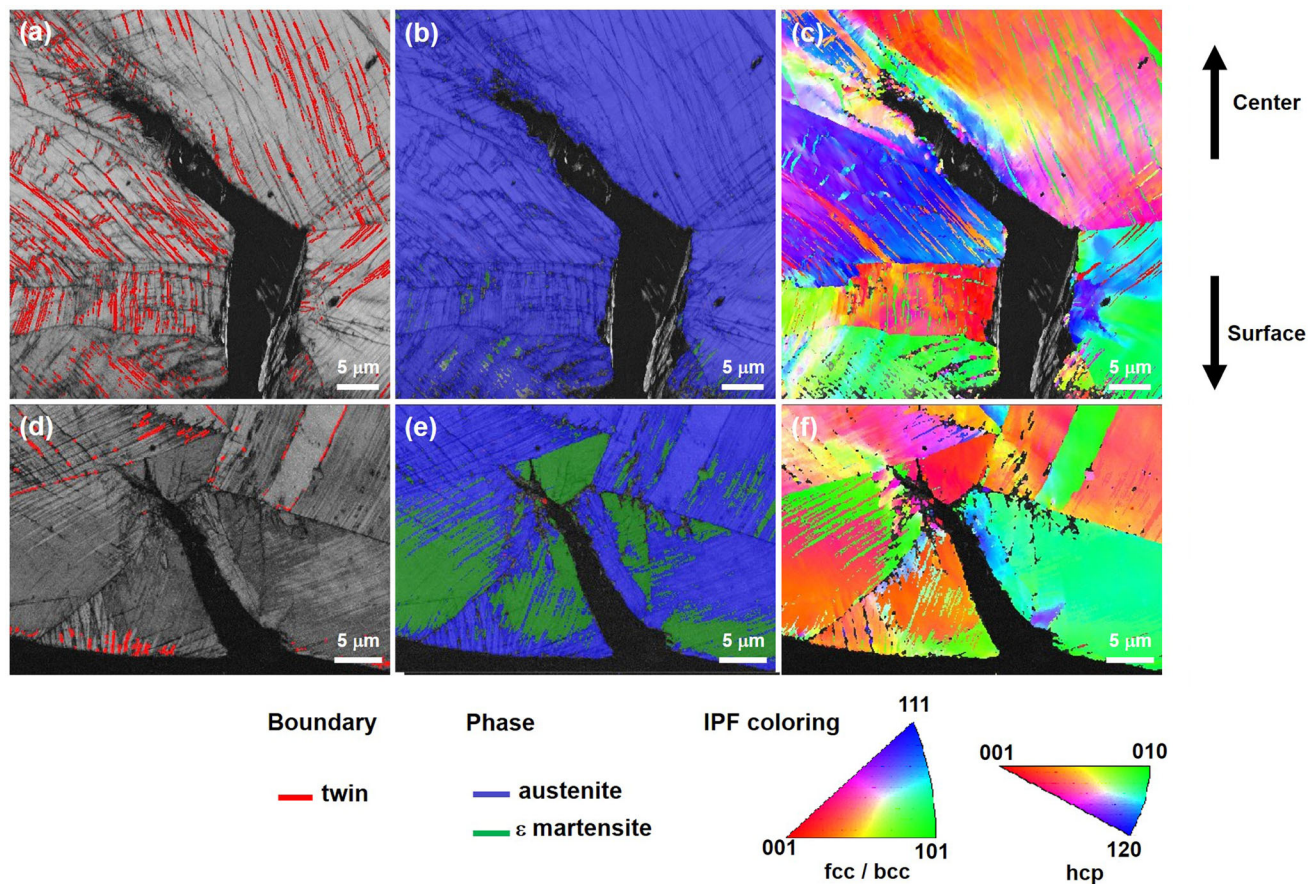


Fig. 5—Crack which appeared within pre-charged C2N2 at true strain = 0.3. (a, d) EBSD band contrast maps showing twin boundaries, (b, e) phase maps, and (c, f) IPF maps.

**Table II. Phase Percentages of Deformed Specimens With and Without Hydrogen Pre-charging**

Sample	$\epsilon$ (Vol Pct)	$\alpha'$ (Vol Pct)
Non-charged, Fractured	0.5	1.1
Pre-charged, 0.1 True Strain	8.3	0.0
Pre-charged, 0.2 True Strain	14.0	0.1
Pre-charged, 0.3 True Strain	14.5	0.0
Pre-charged, Fractured	15.1	0.0

boundaries (Figures 5(a) through (c)) and  $\epsilon$  martensite (Figures 5(d) through (f)) which would be responsible for the transgranular fracture (Figures 2(b) and (c)). Although C2N2 exhibited high austenite stability with  $M_{d30} = -88$  °C,<sup>[22]</sup> the introduction of hydrogen promoted the transformation to  $\epsilon$  martensite during deformation (Table II) because hydrogen decreased the stacking fault energy.<sup>[23,24]</sup> The fraction of  $\epsilon$  martensite increased actively until the true strain of 0.2, and barely increased at higher strains. It seemed that a certain fraction of  $\epsilon$  martensite was needed for the crack propagation. The cracks that propagated along  $\epsilon$  martensite suspended when it reached another grain boundary (Figures 5(d) through (f)). Therefore, the

**Table III. Effective Diffusivity ( $D_{\text{eff}}$ ) and H Content Which Were Measured by Permeation Test and TDA, Respectively**

Alloy	$D_{\text{eff}} (\times 10^{-15} \text{ m}^2 \text{ s}^{-1})$	H Content (Ppm)
C2	2.96	$28.0 \pm 0.6$
N2	1.28	$22.4 \pm 0.8$
C2N2	2.63	$25.6 \pm 0.6$

variation in the depth of brittle fracture (Figures 2(b) and (c)) was in the order of the grain size (50 to 60  $\mu\text{m}$ ).

### C. Hydrogen Diffusion

Electro-chemical permeation tests were conducted to define the depth of hydrogen penetration after hydrogen charging. The results for C2N2 are given in Table III with the data of C2 and N2.<sup>[19,20]</sup> It was expected that C2N2 would exhibit the lowest hydrogen diffusivity since it contained the highest concentration of interstitials, and nitrogen was found to effectively decrease the hydrogen diffusivity.<sup>[20]</sup> However, the diffusivity value of C2N2 was in between those of C2 and N2, and even close to that of C2. Total amount of hydrogen desorbed out during heating the pre-charged samples was  $25.6 \pm$

0.6 ppm, which was also the value between those of C2 and N2. This indicates that carbon–nitrogen interaction would have affected the diffusivity of hydrogen. Unlike in C2N2 and C2, the depth of hydrogen-affected region was uniform in N2.<sup>[20]</sup> By adopting the acquired activation energy for hydrogen diffusion ( $Q$ ) value of the N-containing austenitic stainless steels with the same base composition,<sup>[20]</sup> the hydrogen penetration depth by electro-chemical hydrogen charging could be calculated to be  $\sim 100 \mu\text{m}$  using the following equations:

$$D_{\text{eff}} = D_0 \exp\{-Q/(RT)\}, \quad [1]$$

$$L = \sqrt{2D_{\text{eff}}t}, \quad [2]$$

where  $D_0$  is the maximal diffusion coefficient of hydrogen,  $R$  is the gas constant,  $T$  is the temperature, and  $t$  is the time of hydrogen charging. The estimated depth was higher than the observed depth of brittle fracture zone in the fracture surface (Figures 2(b) and (c))

#### D. Atomic Distribution

Carbon and nitrogen showed unique distributions inside C2N2. Carbon was actively segregated at the grain boundaries (Figures 6(b) and (d)). This was consistent with the results of carbon distribution in C-containing austenitic stainless steels.<sup>[19]</sup> Interestingly, nitrogen also showed segregation at the grain boundary with a less extent (Figures 6(c) and (d)). Considering that nitrogen exhibited no segregation in N-containing austenitic stainless steels,<sup>[25]</sup> it could be assumed that the interaction between carbon and nitrogen must have affected the atomic distribution. When the iso-concentration surfaces of 1.3 at. pct C and 1.0 at. pct N were constructed, carbon clusters were observed but nitrogen was homogeneously distributed (Figure 7).

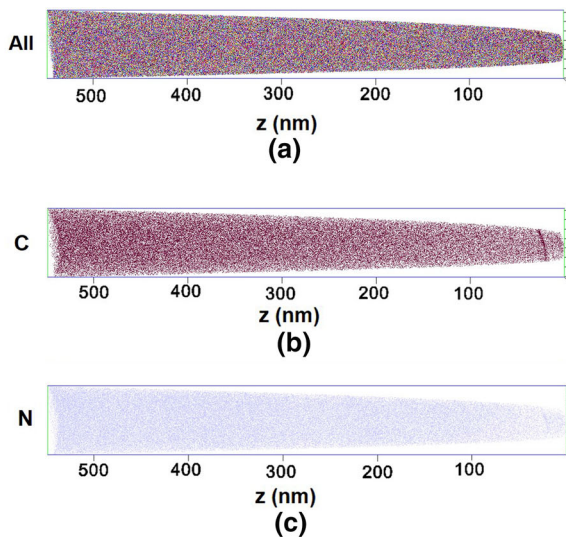


Fig. 6—Atomic distribution in C2N2 obtained by atom probe tomography, showing (a) all atoms, (b) carbon, and (c) nitrogen. (d) The atomic profile of C and N near the grain boundary.

## IV. DISCUSSION

### A. Hydrogen Embrittlement Mechanism

The loss in fracture elongation due to hydrogen originated from the hydrogen-induced cracks formed at the sample surface during deformation. The crack formation at the surface before fracture would induce a notch effect to decrease the overall tensile elongation

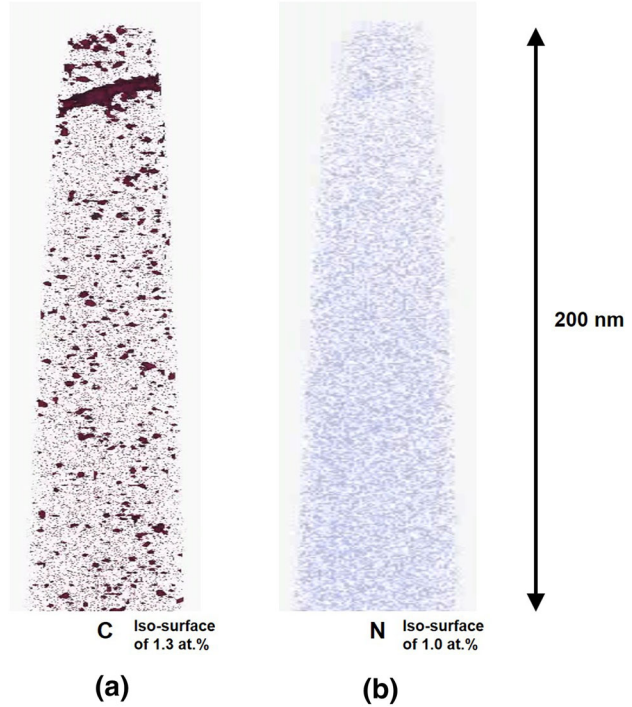


Fig. 7—Iso-concentration surfaces of (a) 1.3 at. pct C and (b) 1.0 at. pct N near a grain boundary.

of the sample. Therefore, the crack initiation and propagation are important in understanding the hydrogen embrittlement mechanism. These processes were affected by the simultaneous introduction of carbon and nitrogen.

### 1. Crack initiation

Alloying carbon and nitrogen simultaneously altered the crack initiation behavior. It is clear that the grain boundaries on the sample surface would contain the highest hydrogen concentration,<sup>[26,27]</sup> and would weaken the bonding strength as Hydrogen-Enhanced DEcohesion (HEDE) theory suggests.<sup>[28,29]</sup> Both the short-range clustering from carbon and short-range ordering from nitrogen are known to induce planar slip during deformation.<sup>[17]</sup> Since short-range ordering or clustering can act as a barrier against the dislocation motion, a dislocation should break the short-range ordering or cluster as it glides on a slip plane. If the broken ordering cannot be restored, the following dislocations would glide on the same plane more easily than other planes; the phenomenon is known as glide plane softening. As a result, dislocation glide is concentrated and strain is likely to be localized on a certain slip. With both elements in solid solution, the slip planarity of the dislocations would become more prominent during deformation than only with either C or N. This is due to the interaction between C and N, which would significantly increase the short-range atomic ordering.<sup>[16,18]</sup> Therefore, stress would be concentrated effectively at the grain boundaries since planar slip would effectively induce dislocation pile-up as shown in the STEM image (Figure 8). This stress concentration would be further supported by hydrogen according to the Hydrogen-Enhanced Localized Plasticity (HELP) theory.<sup>[30]</sup> Moreover, nitrogen segregated to the grain

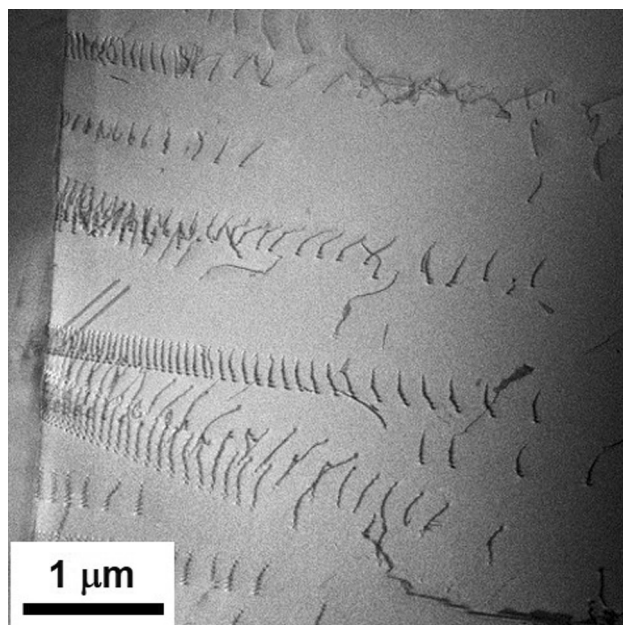


Fig. 8—Planar glide of dislocations in the non-charged C2N2 at 1 pct strain.

boundaries (Figures 6(c) and (d)), and would decrease the grain boundary strength.<sup>[31]</sup> However, the active carbon segregation (Figures 6(b) and (d)) strengthened the grain boundaries to delay the crack initiation.<sup>[19]</sup> Hence, although crack initiation in C2N2 took place in an early deformation stage than in C2 due to nitrogen, the density of the surface cracks at the true strain = 0.1 was less than that in N2 because some grain boundaries were strengthened by C.<sup>[19,20]</sup>

### 2. Crack propagation

Some cracks propagated along the grain boundaries to form intergranular fracture (Figures 2, 5(a) through (c)). In the previous results of N-containing austenitic stainless steels,<sup>[20]</sup> the crack propagation along grain boundaries occurred immediately after the initiation, and the SHR deviation between non-charged and pre-charged alloy was significant before true strain of 0.05. In C2N2, the deviation of SHR also took place at an early deformation stage due to the early crack formation (Figure 1(b)). Nevertheless, the degree of this deviation was smaller than in the N2 (Figure 1(d)). This was because the carbon at the grain boundaries strengthened the region so that the propagation of the cracks along the grain boundaries was impeded (Figures 6(b) and (d)). Larger stress was necessary for the deeper propagation along grain boundaries in C2N2 than in N2.

The cracks also penetrated the grains to form transgranular fracture (Figures 2, 5). As the crack in Figures 5(a) through (c) became deeper, it propagated within the grains and blunted. Since the hydrogen concentration decreases with depth after electro-chemical hydrogen charging,<sup>[27]</sup> twin boundaries would have been more vulnerable for crack propagation than the strengthened grain boundaries. However, due to lower concentration of hydrogen, crack propagation along twin boundaries became inactive as the crack propagated away from the surface. On the other hand, some cracks followed the paths where  $\epsilon$  martensite formed (Figures 5(d) through (f)). The  $\epsilon$  martensite fraction reached the maximum near true strain of 0.2 (Table II). This is the point where the SHR deviation became wider (Figure 1(b)). Since C2N2 exhibited high austenite stability due to both carbon and nitrogen, the propagation along  $\epsilon$  martensite was not as active as in C2.<sup>[19]</sup>

## B. Hydrogen Behavior

The hydrogen diffusivity was found to be reduced by alloying 0.1 to 0.3 wt pct nitrogen.<sup>[20]</sup> On the other hand, carbon over 0.1 wt pct had a negligible effect on hydrogen diffusivity.<sup>[19]</sup> Hydrogen was reported to have an attractive interaction with nitrogen,<sup>[32]</sup> whereas it showed neutral interaction with carbon.<sup>[33]</sup> Since the nitrogen addition is reported to increase the concentration of free electrons, and simultaneous addition of C and N increases it even higher than alloying N alone,<sup>[14]</sup> it can be expected that the hydrogen diffusivity would decrease even greater in C2N2 than in N2. However, the diffusivity of hydrogen in C2N2 was revealed to be close to that in C2 (Table III).

Alloying both carbon and nitrogen was reported to induce different atomic distributions of interstitials than alloying each one alone. From the Mössbauer spectroscopy and Monte Carlo simulation on Fe–C–N alloy, the C–Fe–C 90 deg configuration and N–Fe–N 180 deg configuration which were observed in Fe–C and Fe–N austenite, respectively, were absent in Fe–C–N alloys due to the C–N interaction.<sup>[15,16]</sup> In other words, the interstitials within the first two coordination spheres were strongly repulsive.<sup>[16]</sup> This resulted in stronger short-range atomic ordering in the steels. Thus, the local distortions caused by carbon and nitrogen probably cannot be understood by a simple summation of having carbon or nitrogen alone. Although carbon was still clustered in C<sub>2</sub>N<sub>2</sub> (Figure 7(a)), the atomic distribution of both carbon and nitrogen would be different than in C<sub>2</sub> and N<sub>2</sub>. The segregation of nitrogen at grain boundaries would be evidence for the positive interaction between carbon and nitrogen (Figure 6(c)). Likewise, the positive interaction between hydrogen and nitrogen atoms can be impeded by the presence of adjacent carbon. Therefore, the ability of nitrogen to obstruct the hydrogen diffusion may be not as strong as in N<sub>2</sub>.<sup>[20]</sup>

Since grain boundaries are an effective diffusion path or/and trapping site for hydrogen,<sup>[26,34,35]</sup> it is possible that the trapping energy of the grain boundaries was altered by interstitials and influenced the diffusivity as well as hydrogen embrittlement susceptibility. However, such point cannot be clearly proved by the present study, and further systematic studies are required.

## V. CONCLUSIONS

- (1) Due to electro-chemical pre-charging of hydrogen, brittle fracture occurred in the hydrogen-affected region, which resulted in the degradation of the tensile properties of 15Cr–15Mn–4Ni–0.3Si–0.2N–0.2C (wt pct) steel.
- (2) The grain boundaries at the sample surface were the initiation sites for cracks. The promotion of slip planarity from both carbon and nitrogen, and the weakening of grain boundary strength by nitrogen initiated the cracks at an early deformation stage, but with low density due to the grain boundary strengthening by carbon.
- (3) The cracks propagated in two ways and resulted in a mixed fracture mode of intergranular and transgranular fracture. Some went along the grain boundaries and through the grains along deformation twin boundaries, and the others followed strain-induced  $\epsilon$  martensite. The strengthened grain boundaries by C and enhanced austenite stability by the simultaneous addition of C and N impeded the crack propagation.
- (4) C and N had a positive atomic interaction, which decreased the effect of nitrogen to impede hydrogen diffusion. Thus, hydrogen diffusivity inside the present steel was larger than that in the steel

with only 0.2 wt pct N. However, cracks could not reach the depth that hydrogen penetrated and resulted in lower loss of elongation by hydrogen than steels containing 0.2 wt pct of either C or N.

## ACKNOWLEDGMENTS

This work was supported by the National Research Foundation of Korea (NRF) (Research Project No. 2020R1A2B5B01001900) and Korea Institute of Energy Technology Evaluation and Planning (KETEP) Grant funded by the Korea government (MOTIE) (20203030040020, Fabrication of stainless steel seamless pipes with the tensile strength of 800 MPa for the hydrogen refueling stations).

## DATA AVAILABILITY

The raw/processed data required to reproduce these findings cannot be shared at this time as the data also form part of an ongoing study.

## CONFLICT OF INTEREST

On behalf of all authors, the corresponding author states that there is no conflict of interest.

## REFERENCES

1. M.R. Louthan and R.G. Derrick: *Corros. Sci.*, 1975, vol. 15, pp. 565–77.
2. Y. Yagodzinskyy, O. Todoshchenko, S. Papula, and H. Hänninen: *Steel Res. Int.*, 2011, vol. 82, pp. 20–25.
3. L. Zhang, Z. Li, J. Zheng, Y. Zhao, P. Xu, and C. Zhou: *Int. J. Hydrog. Energy*, 2013, vol. 38, pp. 8208–14.
4. M. Koyama, S. Okazaki, T. Sawaguchi, and K. Tsuzaki: *Metall. Mater. Trans. A*, 2016, vol. 47A, pp. 2656–73.
5. R.P. Reed and M.W. Austin: *Scripta Metall.*, 1989, vol. 23, pp. 1359–62.
6. V.G. Gavriljuk: *Mater. Sci. Eng. A*, 2006, vols. 438–440, pp. 75–79.
7. K.J. Irvine, T. Gladman, and F.B. Pickering: *J. Iron Steel Inst.*, 1969, vol. 119, pp. 1017–28.
8. H.-Y. Ha, T.-H. Lee, C.-S. Oh, and S.-J. Kim: *Scripta Mater.*, 2009, vol. 61, pp. 121–24.
9. Y. Tomota, Y. Xia, and K. Inoue: *Acta Mater.*, 1998, vol. 46, pp. 1577–87.
10. K.-S. Kim, J.-H. Kang, and S.-J. Kim: *Mater. Sci. Eng. A*, 2018, vol. 712, pp. 114–21.
11. B.D. Shanina, V.G. Gavriljuk, H. Berns, and F. Schmalt: *Steel Res.*, 2002, vol. 73, pp. 105–13.
12. H. Berns, V.G. Gavriljuk, S. Riedner, and A. Tyshchenko: *Steel Res. Int.*, 2007, vol. 78, pp. 714–19.
13. F. Schmalt, H. Berns, and V. G. Gavriljuk: *Proc. 7th Int. Conf. High Nitrogen Steels*, Ostend, Belgium, 19–22 September, 2004, pp. 437–46.
14. V.G. Gavriljuk, B.D. Shanina, and H. Berns: *Mater. Sci. Eng. A*, 2008, vols. 481–482, pp. 707–12.
15. V.G. Gavriljuk, B.D. Shanina, and H. Berns: *Acta Mater.*, 2000, vol. 48, pp. 3879–93.
16. A.G. Balanyuk, V.G. Gavriljuk, V.N. Shivanyuk, A.I. Tyshchenko, and J.C. Rawers: *Acta Mater.*, 2000, vol. 48, pp. 3813–21.



17. V. Gerold and H.P. Karnthaler: *Acta Metall.*, 1989, vol. 37, pp. 2177–83.
18. V.G. Gavriljuk, A.I. Tyshchenko, V.V. Bliznuk, I.L. Yakovleva, S. Riedner, and H. Berns: *Steel Res. Int.*, 2008, vol. 79, pp. 413–22.
19. K.-S. Kim, J.-H. Kang, and S.-J. Kim: *Corros. Sci.*, 2021, vol. 180, p. 109226.
20. K.-S. Kim, J.-H. Kang, and S.-J. Kim: *Scripta Mater.*, 2020, vol. 184, pp. 70–73.
21. International Organization for Standardization: *ISO17081. Method of Measurement of Hydrogen Permeation and Determination of Hydrogen Uptake and Transport in Metals by an Electrochemical Technique*, ISO, 2004.
22. K. Nohara, Y. Ono, and N. Ohashi: *Tetsu-to-Hagané*, 1977, vol. 63, pp. 772–82.
23. A.E. Pontini and J.D. Hermida: *Scripta Mater.*, 1997, vol. 37, pp. 1831–37.
24. A. Inoue, Y. Hosoya, and T. Masumoto: *Trans. Iron Steel Inst. Jpn*, 1979, vol. 19, pp. 170–78.
25. K.-S. Kim, J.-H. Kang, and S.-J. Kim: *JOM*, 2020, vol. 72, pp. 2011–2019.
26. G.M. Pressouyre: *Metall. Trans. A*, 1979, vol. 10, pp. 1571–73.
27. Y. Zhao, D.-H. Lee, M.-Y. Seok, J.-A. Lee, M.P. Phaniraj, and J.-Y. Suh: *Scripta Mater.*, 2017, vol. 135, pp. 54–58.
28. A.R. Troiano: *Metallogr. Microstruct. Anal.*, 2016, vol. 5, pp. 557–69.
29. R.A. Oriani: *Annu. Rev. Mater. Sci.*, 1978, vol. 8, pp. 327–57.
30. H.K. Birnbaum and P. Sofronis: *Mater. Sci. Eng. A*, 1994, vol. 176, pp. 191–202.
31. M. Kim, C.B. Geller, and A.J. Freeman: *Scripta Mater.*, 2004, vol. 50, pp. 1341–43.
32. V.G. Gavriljuk, H. Hanninen, A.S. Tereshchenko, and K. Ullakko: *Scripta Metall. Mater.*, 1993, vol. 28, pp. 247–52.
33. S. Simonetti, L. Moro, G. Brizuela, and A. Juan: *Int. J. Hydrog. Energy*, 2006, vol. 31, pp. 1318–25.
34. M. Aucouturier: *J. Phys. Colloq.*, 1982, vol. 43, p. C6-175-186.
35. Y. He, Y. Su, H. Yu, and C. Chen: *Int. J. Hydrog. Energy*, 2021, vol. 46, pp. 7589–7600.

**Publisher's Note** Springer Nature remains neutral with regard to jurisdictional claims in published maps and institutional affiliations.